THE COSMIC-RAY ANTIPROTON FLUX BETWEEN 3 AND 49 GeV

M. Boezio,[1] V. Bonvicini, P. Schiavon, A. Vacchi, and N. Zampa
Dipartimento di Fisica dell'Università and Sezione INFN di Trieste, Via A. Valerio 2, I-34147 Trieste, Italy

D. Bergström, P. Carlson, T. Francke, and S. Grinstein
Royal Institute of Technology (KTH), S-104 05 Stockholm, Sweden

M. Suffert
Centre des Recherches Nucléaires, BP20, F-67037 Strasbourg-Cedex, France

M. Hof, J. Kremer, W. Menn, and M. Simon
Universität Siegen, 57068 Siegen, Germany

S. A. Stephens
Tata Institute of Fundamental Research, Bombay 400 005, India

M. Ambriola, R. Bellotti, F. Cafagna, F. Ciacio, M. Circella, and C. De Marzo
Dipartimento di Fisica dell'Università and Sezione INFN di Bari, Via Amendola 173, I-70126 Bari, Italy

N. Finetti,[2] P. Papini, S. Piccardi, P. Spillantini, and E. Vannuccini
Dipartimento di Fisica dell'Università and Sezione INFN di Firenze, Largo Enrico Fermi 2, I-50125 Firenze, Italy

S. Bartalucci and M. Ricci
Laboratori Nazionali INFN, Via Enrico Fermi 40, CP 13, I-00044 Frascati, Italy

M. Casolino, M. P. De Pascale, A. Morselli, P. Picozza, and R. Sparvoli
Dipartimento di Fisica dell'Università and Sezione INFN di Roma, Tor Vergata, Via della Ricerca Scientifica 1, I-00133 Roma, Italy

J. W. Mitchell, J. F. Ormes, and R. E. Streitmatter
NASA Goddard Space Flight Center, Code 661, Greenbelt, MD 20771

AND

U. Bravar and S. J. Stochaj
Box 3-PAL, New Mexico State University, Las Cruces, NM 88003
Received 2001 March 1; accepted 2001 July 16

ABSTRACT

We report on a new measurement of the cosmic ray antiproton spectrum. The data were collected by the balloon-borne experiment CAPRICE98, which was flown on 1998 May 28–29 from Fort Sumner, New Mexico. The experiment used the NMSU-WiZard/CAPRICE98 balloon-borne magnet spectrometer equipped with a gas Ring Imaging Cherenkov (RICH) detector, a time-of-flight system, a tracking device consisting of drift chambers and a superconducting magnet, and a silicon-tungsten calorimeter. The RICH detector was the first ever flown capable of mass-resolving charge-one particles at energies above 5 GeV. A total of 31 antiprotons with rigidities between 4 and 50 GV at the spectrometer were identified with small backgrounds from other particles. The absolute antiproton energy spectrum was determined in the kinetic energy region at the top of the atmosphere between 3.2 and 49.1 GeV. We found that the observed antiproton spectrum and the antiproton-to-proton ratio are consistent with a pure secondary origin. However, a primary component may not be excluded.

Subject headings: acceleration of particles — balloons — cosmic rays — dark matter —
elementary particles

1. INTRODUCTION

Detailed measurements of the cosmic-ray antiproton energy spectrum provide important information concerning the origin and propagation of cosmic rays in the Galaxy. In fact, antiprotons are a natural product of interactions between cosmic rays and the interstellar matter. Moreover, antiprotons can be produced by exotic sources such as evaporation of primordial black holes (Hawking 1974; Kiraly, Wdowczyk, & Wolfendale 1981; Maki, Mitsui, & Orito 1996) and annihilation of supersymmetric particles (Stecker, Rudaz, & Walsh 1985; Bottino et al. 1998;

Bergström, Edsjö, & Ullio 1999a, 1999b). The measurement of the antiproton spectrum at energies above a few GeV permits the study of these topics free of uncertainties associated with the secondary antiproton production such as nuclear subthreshold effects and of the uncertainties in the solar modulation effect. Furthermore, it permits us to investigate the possible annihilation of heavy supersymmetric particles (Ullio 1999).

Several measurements of the cosmic-ray antiprotons have been performed since the first detection by Golden et al. (1979). However, most of these experiments have measured the antiproton spectrum at energies below 4 GeV (see Orito et al. 2000 and references therein). Only two experiments (Golden et al. 1979; Hof et al. 1996) have obtained antiproton results at energies above 4 GeV, and these results differ by a large amount. We report in this paper a new observation of antiprotons with energies up to 50 GeV

obtained with the CAPRICE98 experiment. This apparatus was launched by balloon from Fort Sumner, New Mexico (34°.3 latitude north, 110°.1 longitude west) and landed close to Holbroke, Arizona (34° latitude north, 104°.1 longitude west), on 1998 May 28 and 29, at an atmospheric pressure of 4.2–6.2 mbar for 21 hr and average value of the vertical cutoff rigidity of about 4.3 GV (Shea & Smart 1983).

Preliminary results on the antiproton-to-proton ratio from CAPRICE98 were reported earlier (Bergström et al. 2000). Here, we present the absolute energy spectrum of antiprotons in the energy region at the top of the atmosphere between 3 and 49 GeV. We also describe in detail the analysis of the flight data. The detector system is described in § 2, the data analysis in § 3 and the results are presented and discussed in § 4.

2. THE CAPRICE98 APPARATUS

Figure 1 shows the NMSU-WiZard/CAPRICE98 spectrometer (Ambriola et al. 1999). It included from top to bottom: a gas Ring Imaging Cherenkov (RICH) detector, a time-of-flight (ToF) system, a tracking system consisting of drift chambers and a superconducting magnet, and a silicon-tungsten imaging calorimeter.

2.1. The Gas RICH Detector

The RICH detector was designed primarily to identify antiprotons in the cosmic rays in a large background of electrons, muons, and pions (Carlson et al. 1994). The RICH detector (Francke et al. 1999; Bergström et al. 2001) consisted of a photosensitive multiwire proportional chamber (MWPC) and a 1 m tall radiator box, filled with high-purity C_4F_{10} gas. When a charged particle with $\beta > 1/n$, where n is the refractive index and $\beta = v/c$ (v being the particle velocity and c the speed of light), passed through the RICH detector, Cherenkov light was emitted in the gas radiator along the

trajectory. The Cherenkov light was emitted at an angle (θ_c) determined by the Cherenkov relation (cos (θ_c) = $[1/(\beta \times n)]$), creating a cone of light in the same direction as the particle trajectory.

The cone of light after traversing the radiator volume was reflected back and focused by a spherical mirror toward the MWPC. There the Cherenkov light interacted with a photosensitive gas, tetrakis-dimethyl-amino-ethylene (also called TMAE), and photoelectrons were produced. These electrons were amplified and then detected by induced pulses in a matrix pad plane. This plane had an area of 51.2×51.2 cm^2, divided in 64×64 pads of size 8×8 mm^2, where the cone of Cherenkov light gave a ringlike image. The size of the ring was dependent on the velocity of the particle. The ring diameter increased from 0 at the RICH threshold (about 18 GV for protons) to about 11 cm for a $\beta \simeq 1$ particle. For $\beta \simeq 1$ charge-one particles, an average of 12 photoelectrons per event were detected.

About half of the particles triggered by the instrument passed through the MWPC, where they ionized the gas. The ionization signals were amplified and detected by the pad plane along with the Cherenkov signals.

2.2. The Time-of-Flight System

The ToF system consisted of two layers of plastic scintillators, one placed above the tracking system and the other below, as indicated in Figure 1. Each layer was divided into two paddles with a size of 25×50 cm^2 and a thickness of 1 cm. The material used was Bicron 401. Each paddle had two 5 cm diameter photomultiplier tubes, one at each end. The distance between the two scintillator layers was 1.2 m.

The signal from each photomultiplier was split in two parts, one was sent to an analog-to-digital converter and the other to a time-to-digital converter. In this way, the ToF system provided both energy loss (dE/dX) and timing information. The scintillator signals also provided the trigger for the data acquisition system.

2.3. The Tracking System

The tracking system consisted of a superconducting magnet and three drift chambers. The average maximum detectable rigidity (MDR) was 330 GV.

The magnet (Golden et al. 1978) consisted of a single coil of 11,161 turns of copper-clad NbTi wire. The outer diameter of the coil was 61 cm and the inner diameter 36 cm. The coil was placed in a dewar filled with liquid helium surrounded by a vacuum shell close in a second dewar filled with liquid nitrogen that reduced the rate of evaporation of liquid helium and enabled attainment of a lifetime of about 100 hr for the superconducting magnet. The operating current was set at 120 A, producing an inhomogeneous field of approximately 4 T at the center of the coil.

The three drift chambers (Hof et al. 1994) used for the trajectory measurements were physically identical. The lateral sides of the chamber box were made from 1 cm thick epoxy-composite plates, while the open top and bottom sides were covered with 160 μm thick copper-plated mylar windows. The inner gas volume of the box was $47 \times 47 \times 35$ cm^3 in size. The drift chamber had six layers, each layer containing 16 27.02 mm wide drift cells, for measurements in the x-directions and four layers for the y-direction. A high efficiency ($\approx 99\%$ for a single drift cell) and an average spatial resolution better than 100 μm were found. The three drift chambers provided a total of 18 posi-

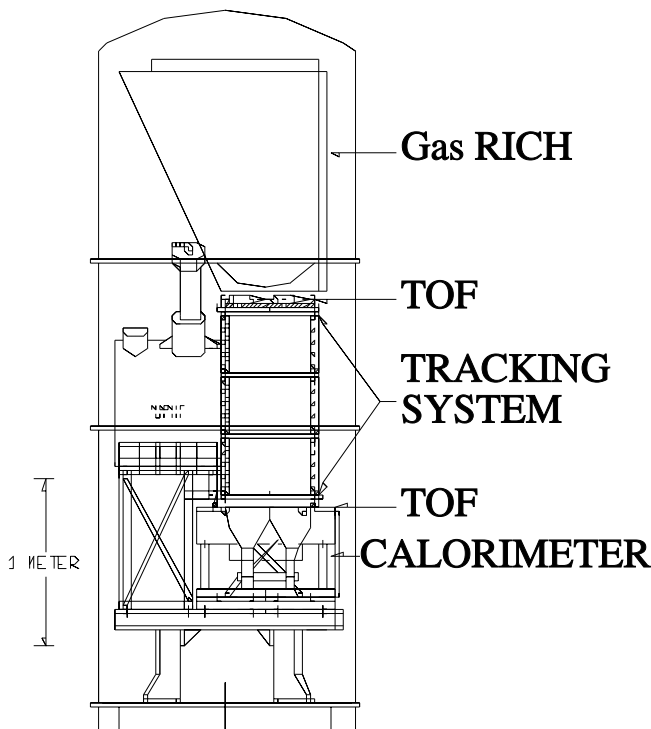
Gas RICH

TOF

TRACKING SYSTEM

TOF

CALORIMETER

1 METER

FIG. 1.—Schematic view of the CAPRICE apparatus

tion measurements in the direction of maximum bending (x direction) and 12 along the perpendicular view (y direction). Using the position information together with the map of the magnetic field, the rigidity of the particle was determined.

2.4. The Calorimeter

The silicon tungsten calorimeter flew in several balloon-borne experiments. The CAPRICE98 configuration was also used in the CAPRICE94 (Boezio et al. 1997) and CAPRICE97 (Kremer et al. 1999) experiments. The calorimeter (Bocciolini et al. 1996; Ricci et al. 1999) was designed to distinguish noninteracting minimum ionizing particles, hadronic cascades, and electromagnetic showers.

The calorimeter consisted of eight 48×48 cm^2 silicon planes interleaved with seven layers of tungsten converter, each one radiation length (X_0) thick. A single plane consisted of an array of an 8×8 pair of silicon detectors. Each detector had a total area of 60×60 mm^2 and was divided into 16 strips, each of width 3.6 mm. The detectors were mounted back-to-back with perpendicular strips to give x and y readouts. The strips of each detector were daisy-chained longitudinally to form one single strip 48 cm long. Taking into account all the material, the calorimeter had a total thickness of $7.2X_0$.

3. DATA ANALYSIS

The analysis was based on 21 hr of data for a total acquisition time of 67,240 s under an average residual atmosphere of 5.5 g cm^{-2}. The fractional live time during the flight was 0.4865 ± 0.0002, resulting in a total live time (T_{live}) of 32712 ± 13 s.

Antiprotons are a very rare component of the cosmic radiation. They must be distinguished from a large background of protons and electrons. Furthermore, products of interactions of cosmic rays in the atmosphere above the payload, such as muons and pions, are a significant background for antiproton measurements performed with balloon-borne experiments. For these reasons strict selection criteria had to be applied on the data acquired from each detector. The rigidity range of the antiproton analysis was 4–50 GV. The lower limit was due to the geomagnetic cutoff of the experiment, while the upper limit was based on the RICH ability to reliably identify antiprotons from other particles at maximum Cherenkov angle ($\beta \simeq 1$). At 50 GV the (anti)proton Cherenkov angle became less than 3 standard deviations away from the Cherenkov angle of $\beta \simeq 1$ particles.

3.1. Antiproton and Proton Selection

3.1.1. Tracking

The primary task of the tracking system was to precisely measure the sign and absolute value of the deflection (1/rigidity) of the particle traversing the apparatus. Events with more than one track, such as products of interactions, were eliminated. For this reason a set of strict selection criteria was imposed on the quality of the fitted tracks. These criteria were based partly on experience gained during the analysis of data from a similar tracking system (Hof et al. 1996; Mitchell et al. 1996; Boezio et al. 1997):

1. At least 12 (out of 18) position measurements in the x direction (direction of maximum bending) and eight (out of 12) in the y direction were used in the fit.

2. There should be an acceptable χ^2 for the fitted track in both directions with stronger requirements on the x-direction.

In addition to these criteria, we required that the value of the deflection, as determined using only the tracking information from the top half of the spectrometer, be consistent with the value determined using only the bottom half of the spectrometer. This additional constraint was imposed on events below the RICH threshold for antiprotons. For events where Cherenkov light was detected (above 18 GV), the particles could be distinguished using the calculated mass. To remove the contamination from spillover protons in the antiproton sample, a concern at high rigidities, we required that the uncertainty in the deflection, estimated on an event-by-event basis, be less that 0.008 (GV)$^{-1}$ (Golden et al. 1991). This value was chosen as a compromise between rejection power for spillover protons and efficiency of the condition in the high-rigidity range. It is worth pointing out that the Cherenkov angle determined by the RICH detector provided an additional check on the deflection (see also § 3.2.5) with a comparable uncertainty at 50 GV.

3.1.2. Scintillators and Time of Flight

The information of the ToF system, with a time resolution of 230 ps, was used to select downward moving particles. The dE/dx information from the top scintillators was used to reject alphas and heavier particles as well as multiparticle events coming from interactions above the top scintillator. This was done by requiring the following two conditions:

1. dE/dx losses in the top scintillator less than 1.8 mip (where a mip is the most probable energy loss for a minimum ionizing particle).
2. Only one paddle hit in the top scintillator plane.

Antiprotons interacting in the calorimeter could produce backscattered particles that traverse the bottom scintillator paddles giving an additional signal. None of these cases significantly affected the performance of the tracking system and calorimeter. Therefore, no restrictions were put on the bottom scintillators.

3.1.3. Calorimeter

The calorimeter was primarily used to identify electrons. The longitudinal and transverse segmentation of the calorimeter combined with the measurement of the energy lost by the particle in each silicon strip resulted in a high-identification power for electromagnetic showers. In the analysis presented in this paper, the calorimeter was used to reject events with electromagnetic showers (see Bergström 2000[3] for a description of the selection criteria), hence reducing the electron contaminations in the antiproton sample. The procedure followed was similar to the one used in the CAPRICE94 antiproton analysis (Boezio et al. 1997). The selection was designed to reject electrons while keeping as large an antiproton fraction as possible.

Figure 2 illustrates the calorimeter performance and shows a schematic view of a 5 GV electron in the

---

[3] Also available at http://www.particle.kth.se/group_docs/astro/research/references.html.
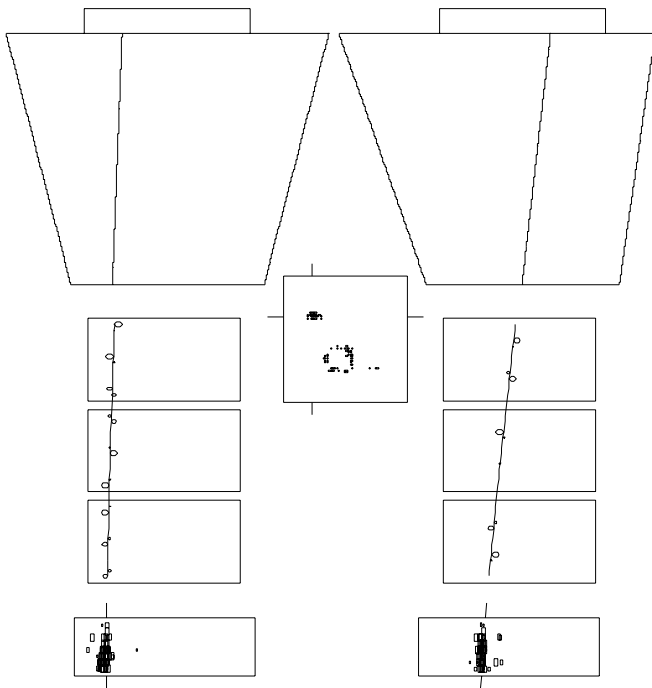
FIG. 2.—Display of a single 5 GV electron in the CAPRICE98 apparatus. The instrument is shown in the view of maximum bending (*x*, *left*) and in the orthogonal view (*y*, *right*). From top to bottom is shown the RICH seen from the side with a view of the signals in the pad plane (*center square*), the tracking stack of three drift chambers, and the imaging calorimeter at the bottom. Note that the figure is not to scale. The calorimeter is significantly thinner than it is shown in the figure. The RICH shows the detected Cherenkov ring typical of a $\beta \simeq 1$ particle well separated from the ionization cluster of pads. A line is drawn through all instruments that is the fitted track of the particle. In the drift chambers along that line there are small circles drawn for each wire that gave a signal. The size of the circle is proportional to the calculated drift time for the electrons at that wire. The calorimeter shows the typical signature of an electromagnetic shower induced by the electron.
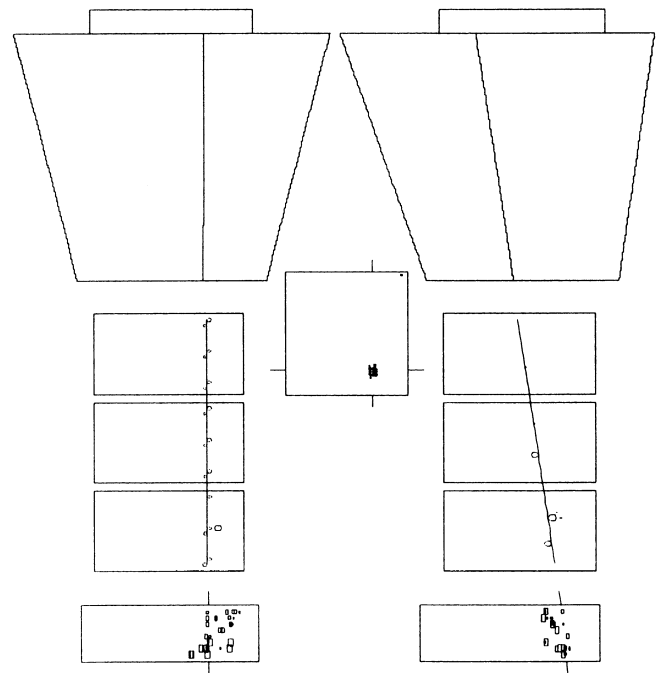

FIG. 3.—Same as Fig. 2, but for a 6.4 GV antiproton traversing the CAPRICE98 apparatus. No Cherenkov light is detected in the RICH pad plane where the ionization cluster can be seen. The antiproton interacts in the calorimeter, showing several charged particles emerging from the vertex of interaction.

3.1.4. RICH

The RICH detector was used to measure the Cherenkov angle of the particles and hence their velocities. Below the threshold rigidity for antiprotons to produce Cherenkov light in the gas (about 18 GV), the detector was used as a

CAPRICE98 apparatus. In the figure there are left and right views, symbolizing, respectively, the *x* and *y* views of the CAPRICE98 apparatus. At the top is the RICH detector, and a rotated view of the signals in the pad plane of the MWPC is shown in the square frame in the center of the figure. The ionization cluster of pads can be seen well separated from the Cherenkov ring typical of a $\beta \simeq 1$ particle. The three central boxes are the drift chambers of the tracking system. At the bottom there is a rectangular frame that symbolizes the calorimeter. The line that is drawn through all detectors represents the fitted track of the particle. Along the line in the drift chambers there are small circles drawn around each wire that gave a signal. The size of the circle is proportional to the calculated drift time for the electrons at that wire. The calorimeter shows the electromagnetic shower induced by an electron.

The electromagnetic shower in the calorimeter of Figure 2 is clearly distinguishable from the hadronic shower produced by an interacting antiproton candidate shown in Figure 3 and from the noninteracting pattern of another antiproton candidate shown in Figure 4.

Out of the 31 antiproton events surviving all antiproton selections, eight were found to have interacted in the calorimeter. This is in agreement with the simulated expectation of 9.7 ± 1.7 antiproton interactions in the calorimeter.
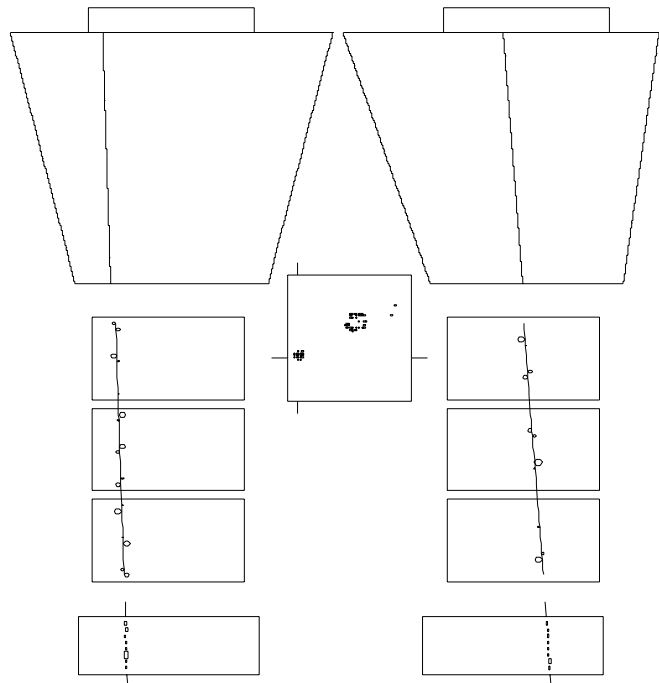

FIG. 4.—Same as Fig. 2, but for a 22.7 GV antiproton traversing the CAPRICE98 apparatus. The calorimeter shows the typical pattern of a noninteracting particle.

threshold device to veto lighter particles, while above it the Cherenkov angle was reconstructed. Below 25 GV the fluctuations in the number of detected photoelectrons were quite large owing to variations in threshold rigidity caused by pressure variation in the radiating gas and because of large Poisson fluctuations as the average number of photoelectrons detected at this rigidity was 6 GV. Therefore, antiprotons in the rigidity range 4 to 25 GV were selected if the event did not produce a Cherenkov signal or when the reconstructed Cherenkov angle was consistent with that of an antiproton with the measured rigidity.

We show in Figure 5 the separation between antiprotons and lighter particles, after applying tracking, ToF, and calorimeter selection criteria, by means of the RICH information in the rigidity range from 4 to 18 GV. The events in Figure 5 are plotted as a function of the base 10 logarithm of the number of pads (n) used for the reconstruction of the Cherenkov angle (Bergström 1999[4]; Bergström et al. 2001) plus 1. It can be noted from the top panel that protons have low values of n (note the logarithmic scale on the y axis), 93% being at zero, while on the negative side a corresponding peak can be seen indicating the antiprotons. It is evident from the figure that faster particles (mostly muons and pions) at higher n can clearly be separated from the antiprotons. In the analysis, (anti)protons below 25 GV were selected by requiring a value of n equal to 0. In this way 26 antiprotons were identified. These events had rigidities between 4 and 17 GV. Note that events were also selected if the Cherenkov angle could be constructed, and three events were identified below 25 GV.

It is worth noting that when using the RICH detector as a threshold device the tracking system gave information about where in the pad plane the Cherenkov light should have been detected, thereby greatly enhancing the detector

---

[4] Also available at http://www.particle.kth.se/group_docs/astro/research/references.html.
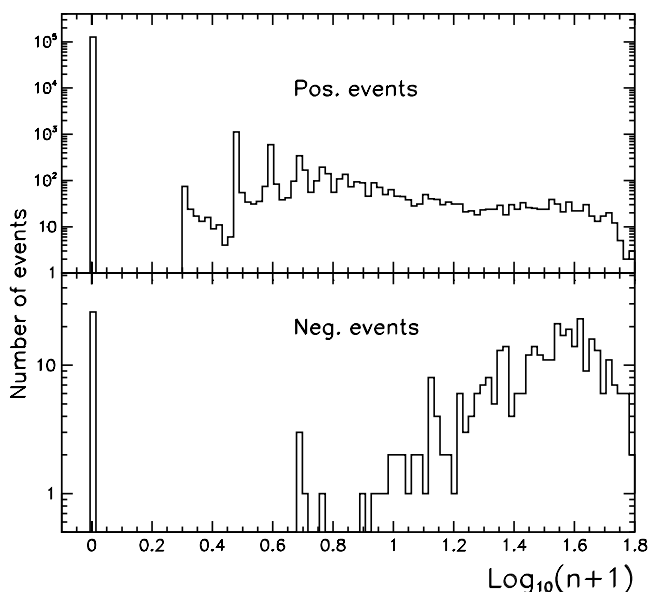
immunity to noise. The number of noisy pads per event was, on average, less than one out of 4096 channels pads^{-1}. This allowed a stringent selection to be applied for antiprotons where no signals should appear in the predicted area and yet maintaining a high-identification efficiency. All 4096 channels were working during the entire flight.

Figure 3 shows the schematic view of a 6.4 GV selected antiproton. At this rigidity the antiproton does not produce light, and, in fact, only the signal from the ionization owing to the crossing particle is detected in the pad plane.

Since the RICH detector played a crucial role in the rejection of background muon and pion events, stringent selection criteria were applied to the RICH data for the events above the antiproton threshold. The Cherenkov angle resolution for protons was determined using a large sample of protons selected using the calorimeter and scintillators. The resolution varied from 11 mrad at threshold to about 1.3 mrad for fully relativistic protons (Bergström et al. 2001). Figure 6 shows the measured Cherenkov angle as a function of rigidity. The events were selected from the flight data after applying tracking and ToF selection criteria. The solid, dotted, and dashed lines indicate the calculated Cherenkov angle for muons, kaons, and (anti)protons, respectively. Five antiprotons are clearly identified, and they are shown with black boxes and with 1 standard deviation error bars for both the rigidity and Cherenkov angle measurements.

In conclusion, the conditions on the RICH detector information used for the antiproton selection were as follows:

FIG. 5.—Distribution of base 10 logarithm of the number (n) of pad used in the Cherenkov angle calculation plus 1 for positive and negative particles passing the tracking, ToF, and calorimeter selection criteria in the rigidity range from 4 to 18 GV.
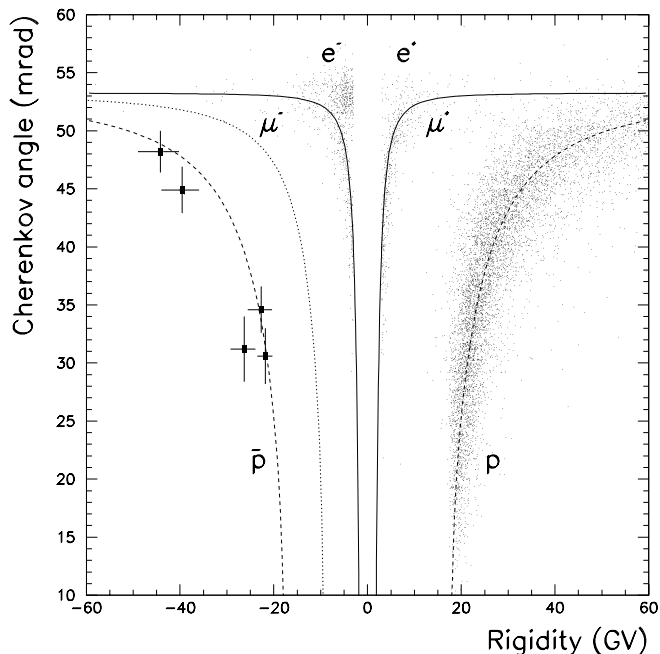

FIG. 6.—Measured Cherenkov angle for singly charged particles passing the tracking and ToF selection criteria (8086 events) as a function of rigidity. The solid, dotted, and dashed lines represent the theoretical values of the Cherenkov angle for muons, kaons, and (anti)protons, respectively. To the right is a dense band of protons starting at approximately 18 GV and extending to higher energies and increasing Cherenkov angles. The main bulk of electrons and positrons were located at the low energies (below 10 GeV) and at maximum Cherenkov angle. On the negative side, the location of five antiprotons between 20 and 50 GV are indicated with black squares together with 1 standard deviation errors on the measured rigidities and Cherenkov angles.

1. The center, extrapolated from the tracking information, of the Cherenkov ring was required to be contained in the pad plane.

2. Multiple charged tracks traversing the MWPC were rejected by requiring that there be only one cluster of pads with a high signal, typical of ionization from a charged particle in the location indicated by the tracking system.

3. If the particle crossed the MWPC (46% of the events), a good agreement between the particle's impact position as determined by the RICH and the tracking system was required. The difference in x and y should be less than 3 standard deviations (rigidity dependent), typically less than 5 mm.

4. Conditions on the Cherenkov angle for events were as follows:

a) Between 4 and 25 GV, there was no signal due to Cherenkov light.

b) However, the following criteria were met for all rigidities above the antiproton threshold (calculated on an event by event base according to the measured gas pressure [Bergström et al. 2001]):

i) A rigidity dependent condition on the number of pads used for the reconstruction of the Cherenkov angle was applied. The condition required more than 5 pads at the antiproton threshold increasing to 20 above 35 GV.

ii) The reconstructed Cherenkov angle should not deviate by more than 3 standard deviations below and 2 standard deviations above from the expected Cherenkov angle for (anti)protons.

iii) To suppress the background from lighter particles, the reconstructed Cherenkov angle was required to be more than 4 mrad (3 standard deviations for $\beta \simeq 1$ particles) away from the expected Cherenkov angle for pions (about 53 mrad above 18 GV).

Hence, between the antiproton threshold (about 18 GV) and 25 GV, antiprotons were selected either if the event did not produce a Cherenkov signal or if the reconstructed Cherenkov angle was consistent with that of an antiproton with the measured rigidity.

Figure 4 shows the schematic view of one of the selected antiprotons. The clean Cherenkov ring in the RICH pad plane is well separated from the ionization cluster of pads, thus permitting the mass associated with the event to be reconstructed.

3.2. Contamination

The contamination owing to e^-, μ^-, π^-, and spillover protons in the antiproton sample was studied carefully using simulations and experimental data taken during the flight and on the ground before the flight.

3.2.1. Albedo particles

Albedo particles were rejected using the ToF information. With a ToF between the top and bottom scintillators of more than 4 ns, the 0.23 ns resolution ensured a negligible background of upgoing particles.

3.2.2. Electron Contamination

The calorimeter performance was studied primarily with simulations. Simulation studies showed that electron contamination in the calorimeter selection was of 0.6% ± 0.2%

independent of rigidity in the interval from 4 to 50 GV. This value was cross-checked by studying electrons selected using a condition on the total number of strips hit in the calorimeter. It is worth noting that only the calorimeter was able to separate electrons from muons above about 5 GV.

The electron contamination in the RICH selection was studied using a sample of 495 e^- in the interval 4–50 GV (478 between 4 and 18 GV), selected using the calorimeter. Of the 495 events one was selected as antiproton resulting in an electron contamination of $0.20\%^{+0.47\%}_{-0.17\%}$ in the RICH selection for antiprotons.

To estimate the electron background, we considered the events with negative curvature between 4 and 50 GV. After imposing the tracking and ToF selection criteria to this sample, 1031 negative events were left. As a worst case, we assumed that all of these events were electrons. Applying the rejecting power of the RICH and calorimeter to this sample resulted in an electron contamination of less than 0.1 event over the entire range of the antiproton measurement. Hence, the electron contamination in the antiproton sample can be assumed negligible.

3.2.3. Muon Contamination

The calorimeter cannot separate muons from noninteracting antiprotons. The antiproton identification in a muon background was performed by the RICH. The muon contamination in the RICH selection was studied using a sample of muons collected during a ground data run prior to the launch. The fraction of muons surviving the antiproton RICH selection was $0.36\%^{+0.13\%}_{-0.10\%}$ between 4 and 8 GV, $0.30\%^{+0.18\%}_{-0.12\%}$ between 8 and 18 GV, $0.76\%^{+0.60\%}_{-0.36\%}$ between 18 and 30 GV and $1.7\%^{+1.4\%}_{-0.8\%}$ between 30 and 50 GV. Defining negative muons all the events surviving the tracking, ToF, and calorimeter antiproton selection criteria, 319, 108, 24, and 11 muons were selected from the flight data between 4 and 8 GV, 8 and 18 GV, 18 and 30 GV, and 30 and 50 GV, respectively. Multiplying these numbers by the surviving fractions found above and taking into account the presence of antiprotons in the sample, the muon contamination in the antiproton sample was estimated to be $1.1^{+0.4}_{-0.3}$ in the first rigidity bin, $0.28^{+0.17}_{-0.11}$ in the second, $0.15^{+0.12}_{-0.07}$ in the third and $0.10^{+0.15}_{-0.08}$ in the forth. This contamination was later subtracted from the antiproton signal and is shown in parentheses in Table 1.

3.2.4. Meson Contamination

Pions started to produce light in the gas-RICH detector above ~ 3 GV. Since the RICH is a β-detector, the pion contamination was studied by scaling the muon sample. The contamination was similar to that of muons except in the first bin where it was 0.6% ± 0.1%. However, pions were a small component compared to muons in the flight data. Between 3 and 4 GV pions could be clearly identified by the gas-RICH, and it was found that pions were 12% ± 2% of the muons. Assuming that a similar value is valid for the bin 4–8 GV, the resulting pion plus muon contamination in the antiproton sample in this bin was $1.17^{+0.35}_{-0.27}$.

Theoretical calculations (Stephens 1981) of the kaon spectrum in the atmosphere indicate that the kaon-to-antiproton ratio is about 2%. Hence, they are a negligible contamination of the antiproton sample. Furthermore, above ~ 9 GV, kaons are suppressed by the RICH selection. It is worth pointing out that, as can be seen in Figure 6 (*dotted*

TABLE 1

SUMMARY OF ANTIPROTON RESULTS

Rigidity at the Spectrometer (GV)	Observed Number of Events at Spectrometer[a]	Extrapolated Number at Top of Payload	Atmospheric Secondaries	Extrapolated Number of Primary Events at TOA
4.0–8.0	15(1.17)	$25.9^{+9.6}_{-7.3}$	6.73	$21.1^{+10.5}_{-8.0}$
8.0–18.0	11(0.28)	$20.1^{+8.4}_{-6.1}$	4.43	$17.0^{+9.2}_{-6.7}$
18.0–30.0	3(0.15)	$7.4^{+7.7}_{-4.3}$	1.16	$6.8^{+8.3}_{-4.7}$
30.0–50.0	2(0.14)	$7.8^{+11.6}_{-5.7}$	0.547	$7.8^{+12.5}_{-6.1}$

[a] The numbers shown in parentheses are the estimated background events owing to muons, pions and, in the highest energy bin, also spillover protons.

line), no negative kaons were identified between 9 and 50 GV.

3.2.5. *Spillover Proton Contamination*

Spillover protons can represent a nonnegligible contamination in the antiproton sample above 20 GV. To obtain the shape of the spillover proton distribution a Monte Carlo approach was used. We started with an input power-law spectrum in rigidity that was transformed in deflection and smeared with values randomly picked from the resolution function. The spectral index for the power law was obtained from the proton spectrum measured by CAPRICE98 above 20 GV and was found to be −2.74 ± 0.02.

The resolution function was obtained from a measurement of straight tracks taken at ground prior to the flight without the magnetic field. These were analyzed as if they were high-rigidity events with magnet on. In this case the resolution function is simply the deflection distribution. To construct this distribution, events that suffered multiple Coulomb scattering had to be eliminated since they could enlarge the distribution (see Menn et al. 2000). In fact, the multiple scattering affected events essentially at low energy, while spillover events were due to high-energy protons. This was done by requiring a Cherenkov light signal along with high value of the measured Cherenkov angle in the RICH so as to select close to fully relativistic events (mostly muons and electrons). Then electrons were eliminated using the calorimeter. The large majority of the selected events were particles (muons) with rigidity greater than 5 GV.

The simulated proton spillover distribution was normalized with the experimental deflection distribution between −0.02 and 0 (GV)$^{-1}$ and used to obtain an estimation of the experimental proton spillover distribution. Figure 7 shows the experimental distribution with the estimated proton spillover contribution (*solid line*). The distribution includes spillover protons, muons, and antiprotons. The events for the deflection distribution were selected from the whole flight data set with the complete antiproton selection (tracking, ToF, RICH, and calorimeter conditions) except for the condition on the reconstructed Cherenkov angle. At the smallest deflections (high rigidities) the dominant component was the spillover protons.

Finally, the contamination of spillover protons was determined from this calculation by integrating the experimental spillover distribution over the proper deflection range. Between 0 and 30 GV the estimated spillover contamination was less than 0.002 events, and between 0 and 50 GV it was about 0.39. However, this was not the real spillover contamination in the antiproton sample since antiprotons above the threshold of the RICH detector were selected with the additional condition on the measured Cherenkov angle. For the rigidity range from the threshold of the RICH detector up to 50 GV, the spillover proton contamination was obtained by calculating the probability that the 0.39 spillover protons previously estimated were selected with the Cherenkov angle condition. This probability was obtained using negative events with deflection smaller than 0.01 GV^{-1} (i.e., essentially spillover protons). Using this process, we derived that the contamination of spillover protons was 0.04 events below 50 GV.

3.3. *Efficiency*

The antiproton selection efficiencies were studied using a large sample of experimental protons from flight data set. It was assumed that protons and antiprotons had the same efficiencies in the RICH, scintillators, and the tracking system. However, in the calorimeter the efficiencies were not assumed to be the same because of the difference in the interaction cross sections. Hence, the calorimeter efficiency for protons and antiprotons was studied using simulations.

The tracking efficiency was studied with two independent methods (see Bergström 2000). Both were based on track reconstruction codes that were independent of the drift chamber tracking system and used information from the
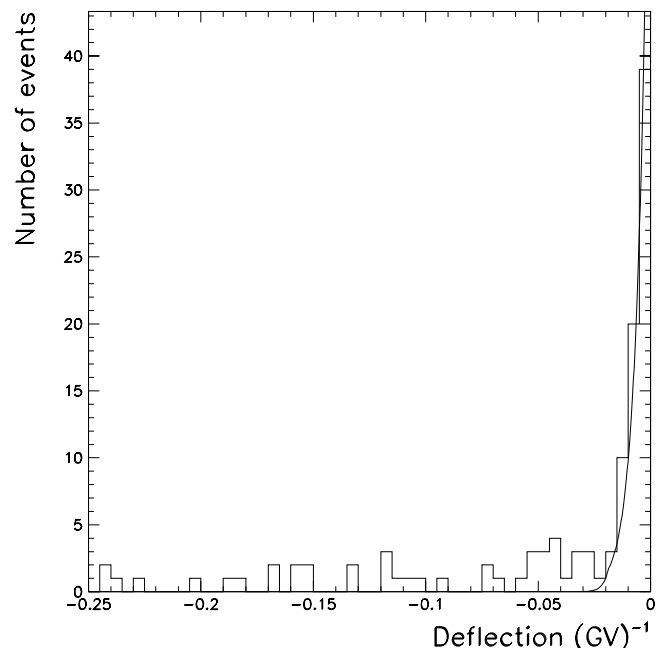

FIG. 7.—Deflection distribution from flight data selected with all antiproton conditions except requirements on the Cherenkov angle. The solid line is a fit of the proton spillover contribution.

other available detectors. The first method used the position of the ionization cluster in the MWPC of the RICH detector, information from the two ToF scintillation detectors (only in the *x* direction), and from the electromagnetic calorimeter to reconstruct the track of the particle traversing the detector system. This combination had an estimated MDR of 4.5 GV. The second method used the RICH to determine the rigidity from the velocity derived from the Cherenkov angle measurement with the help of an extrapolated straight track from the calorimeter.

The two methods were tested with muons from ground data, and similar results were obtained between 0.2 and 10 GV. With flight data, the first method sampled the tracking efficiency of protons below 10 GV while the second above 18 GV (because of the gas-RICH threshold). In this case the efficiencies differed by $\simeq 6\%$. From previous experience with a similar tracking system (Boezio et al. 1999), the proton tracking efficiency was expected to reach a plateau above 2 GV. This seems in disagreement with what found here. However, the first method could be biased by contamination of secondary low-energy protons that would not affect the second method (for more details see Bergström 2000). Thus, the efficiency of the tracking selection was obtained by the second method for the rigidity range from 4 to 50 GV (Fig. 8, *dotted line*). The difference found between the proton tracking efficiency with the two methods was considered a systematic uncertainty, and a 6% systematic uncertainty was included in the flux calculation for rigidities between 4 and 20 GV.

Secondary particles backscattering from the calorimeter could result in an inefficiency for the tracking selection. We studied this effect selecting from the flight data events that interacted in the calorimeter producing large signals (above 1.8 mip) in the bottom scintillator. For these events we applied the tracking selection. Accounting for the relative abundance of these events, we found an overall decrease in the tracking efficiency of about 0.4%.

A Monte Carlo simulation based on the CERN GEANT/FLUKA-3.21 code (Brun et al. 1994) was used to study the calorimeter selection efficiencies. Results from similar simulations were found to be in good agreement with test beam data and experimental results from previous balloon flights (Bocciolini et al. 1993; Boezio 1998[5]). It was found that the efficiency for the selection of antiprotons and protons using simulated data were in agreement, within the statistical uncertainties. The calorimeter efficiency for protons selected from experimental data was in reasonable agreement with previous simulations. Differences (about 2%) found were probably due to the less accurate simulations of hadronic showers compared to electromagnetic showers. Since simulations indicated that protons' and antiprotons' calorimeter selections had the same efficiency, the efficiency of the experimental proton calorimeter selection was also used for the antiprotons (Fig. 8, *dashed line*).

The RICH efficiency was rigidity dependent and is shown as a solid line in Figure 8. As expected, the efficiency was constant below the gas-RICH threshold, but it started decreasing at 14 GV owing to above threshold protons that spilled down to lower rigidities because of the finite resolution of the tracking system. Above 25 GV the antiprotons were selected only with conditions on the Cherenkov angle. The decrease of the RICH efficiency above 30 GV was caused by the requirement that the Cherenkov angle should be more than 4 mrad away from the expected Cherenkov angle for pions.

Since the detector efficiencies varied with rigidity, mean efficiencies had to be calculated. This was done by weighting the efficiencies in each bin with the proton spectrum measured in this experiment (with a larger number of bins and no RICH selection) and with an antiproton spectrum given by interstellar secondary calculation by L. Bergström & P. Ullio (1999, private communication), which included the effects if the geomagnetic cutoff.

3.4. *Geometrical Factor*

The acceptance of the instrument allowed for particles with a range of zenith angles to be measured. The maximum angle was 14°, and the mean of the distribution was at 8°.

The geometrical factor was obtained with Monte Carlo techniques (Sullivan 1971) and the same track-fitting algorithm used in this analysis to trace the particles through the spectrometer. The geometrical factor (G) was found to be constant at 155.0 ± 1.1 cm^2 sr in the rigidity range from 4 to 50 GV.

3.5. *Payload and Atmospheric Corrections*

3.5.1. *Payload Corrections*

To determine the number of particles at the top of the payload, the losses and the production of particles owing to interaction in the material of the payload had to be considered. To reach the tracking system of the spectrometer, the particles had to go through first the aluminum shell of the payload, the RICH detector, and then the top scintillator of the ToF system. It was assumed that all particles that interacted above the tracking system were rejected by the selection criteria. The probability of an interaction in the material of the drift chambers that would not be rejected
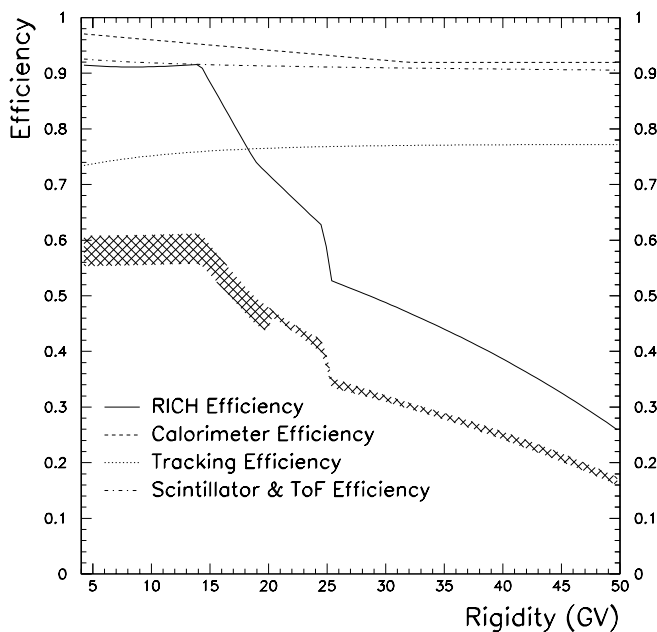

FIG. 8.—Efficiencies for the different detectors of the magnet spectrometer for detecting antiprotons. The hatched area indicates the 1 standard deviation confidence interval of the combined efficiency.

by the tracking system conditions was considered as being negligible. The data were corrected for these losses with multiplicative factors, using the expression for the interaction mean free path for the different materials in the detectors given by Stephens (1997). This gave correction factors of 1.132, 1.118, 1.109, and 1.104 for antiprotons and of 1.081, 1.082, 1.084, and 1.086 for protons in the four rigidity intervals. The corrected number of antiprotons and protons at the top of the payload are given in Tables 1 and 3.

3.5.2. Atmospheric Corrections

For the production of secondary antiprotons and protons in the atmosphere, we used the calculation by Papini, Grimani, & Stephens (1996) for the protons and the calculation by Stephens (1997) for the antiprotons. To determine the secondary spectra we compared our measured proton spectrum propagated to the top of the atmosphere with the spectrum used for the secondary calculations at solar minimum (Papini et al. 1996; Stephens 1997) from which a normalization factor was derived. The resulting secondary fluxes were normalized with the geometrical factor and live time of the experiment and subtracted from the corrected numbers using a mean residual atmosphere of 5.5 g cm^{-2}. The number of atmospheric antiprotons and protons are given in Tables 1 and 3.

The correction for losses in the atmosphere was carried out using a method analogous to the instrument correction. This gave correction factors of 1.1, 1.089, 1.082, and 1.079 for antiprotons and of 1.061, 1.063, 1.064, and 1.065 for protons in the four rigidity intervals.

3.6. Geomagnetic Transmission Correction

To be able to get the fluxes at the top of the atmosphere, the transmission of the particles through the Earth's magnetic field had to be taken into account. During the flight the position of the payload changed between 34°.3 and 35°.5 latitude north and between 104°.1 and 110°.1 longitude west. This correspond to an average value of the vertical cutoff rigidity of about 4.3 GV (Shea & Smart 1983). However, this cutoff is not a sharp value below which all particles are deflected and cannot reach the apparatus and above which all particles arrive. In fact, around the geomagnetic cutoff, the particles are partially transmitted through the Earth's magnetic field. Furthermore, the penumbral bands define forbidden bands of rigidity, which vary with arrival direction, time, and geographic location. In this analysis all these effects are represented by a transmission function that was derived by the experimental data.

We found that the CAPRICE94 (Boezio et al. 1999) and CAPRICE98 proton spectra above about 10 GeV are nearly identical in shape, and the absolute fluxes differ by

$\simeq 7\%$, in good agreement considering both the statistics and systematic errors, which in Boezio et al. (1999) were estimated to be on the order of 10%. Moreover, the solar modulation during the two balloon flights was also very similar. The values from the neutron monitor counter CLIMAX[6] (Simpson & Pyle 1996) were 415,600 and 417,000 counts hr^{-1} at the time of the CAPRICE94 and CAPRICE98 flights, respectively. However, the CAPRICE94 experiment took place in North Canada at an average geomagnetic cutoff of about 0.5 GV. Hence, above 1 GV the effects of the geomagnetic field on the CAPRICE94 proton spectrum were negligible. Consequently, the transmission function was defined as the ratio between the experimental CAPRICE98 and CAPRICE94 proton fluxes.

The correction factors (TF) for the geomagnetic effect were derived weighting the transmission function with the proton and antiproton spectra as done for the efficiencies. The resulting transmission values differ by only 1 in the first bin (4–8 GV) where they are 0.84 ± 0.06 and 0.81 ± 0.07 for antiproton and protons, respectively.

4. RESULTS

4.1. Antiproton Flux at the Top of the Atmosphere

Given the number of events ($N_{\bar{p}}^{\rm TOA}$) selected with the antiproton criteria and corrected for selection efficiencies, losses in the payload and in the atmosphere and atmospheric secondaries, we obtained the antiproton fluxes at the top of the atmosphere from the relation,

$$\text{Flux}(E) = \frac{1}{T_{\rm live}\, G\, \Delta E\, TF}\, N_{\bar{p}}^{\rm TOA}(E)\,,$$

where ΔE is the energy bin corrected for ionization losses to the top of the atmosphere and E the kinetic energy. The resulting antiproton flux is given in Table 2. The total errors include both statistical and systematic errors. The mean energies of the bins are given according to Lafferty & Wyatt (1995).

Figure 9 shows the antiproton flux measured by this experiment together with other experimental data (Buffington, Schindler, & Pennypacker 1981; Mitchell et al. 1996; Boezio et al. 1997; Basini et al. 1999; Orito et al. 2000). The two solid lines show the upper and lower limit of a calculated flux of interstellar secondary antiprotons (Simon, Molnar, & Roesler 1998) using a recently measured proton and helium spectra (Menn et al. 1997) and a reacceleration model that allows energy-changing processes caused by the nonannihilation process and by elastic scattering. The dashed line shows the interstellar secondary antiproton flux calculated by L. Bergström & P. Ullio (1999, private communication). This calculation assumed a diffusion model of propagation with an isotropic diffusion coefficient and no reacceleration. It used the interstellar proton spectrum measured by the CAPRICE94 experiment (Boezio et al. 1999). The dotted line shows the primary antiproton flux by Ullio (1999), which included a minimal supersymmetric standard model (MSSM) with a contribution from an assumed Higgsino-like neutralino, with a mass of 964 GeV. The theoretical fluxes, but not the experimental

TABLE 2
ANTIPROTON FLUXES AT THE TOP OF THE ATMOSPHERE (TOA)

Kinetic Energy at TOA (GeV)	Mean Kinetic Energy at TOA (GeV)	Antiproton flux at TOA [(m² sr s GeV)$^{-1}$]
3.19–7.14	4.97	$(12.6^{+6.3}_{-4.8}) \times 10^{-3}$
7.14–17.11	11.09	$(3.4^{+1.8}_{-1.3}) \times 10^{-3}$
17.11–29.10	22.19	$(1.1^{+1.4}_{-0.8}) \times 10^{-3}$
29.10–49.09	37.44	$(0.77^{+1.23}_{-0.60}) \times 10^{-3}$

TABLE 3

ANTIPROTON-TO-PROTON RATIO AT THE TOP OF THE ATMOSPHERE (TOA)

RIGIDITY AT SPECTROMETER (GV)	OBSERVED NUMBER OF EVENTS[a]		EXTRAPOLATED NUMBER[b] AT TOP OF PAYLOAD		ATMOSPHERIC SECONDARY		$\bar{p}/p$ AT TOA
	$\bar{p}$	p	$\bar{p}$	p	$\bar{p}$	p	
4.0–8.0	15(1.17)	85331	15.66	92201	4.06	2546	$(1.3^{+0.6}_{-0.5}) \times 10^{-4}$
8.0–18.0	11(0.28)	39185	11.98	42417	2.64	855	$(2.3^{+1.2}_{-0.9}) \times 10^{-4}$
18.0–30.0	3(0.15)	5765	3.16	6251	0.49	113.8	$(4.4^{+5.4}_{-3.0}) \times 10^{-4}$
30.0–50.0	2(0.14)	1458	2.05	1583	0.14	29.0	$(1.2^{+2.0}_{-1.0}) \times 10^{-3}$

[a] The numbers shown in brackets are the estimated background events owing to muons, pions and, in the highest energy bin, also spillover protons.

[b] The corrections to the top of the payload account only for loss of particles in the apparatus.

values of the other experiments, were corrected for the solar modulation conditions corresponding to the CAPRICE98 flight using a spherically symmetric model (Gleeson & Axford 1968) with a solar modulation parameter of $\Phi = 600$ MV.

4.2. Antiproton-to-Proton Ratio

To obtain the antiproton-to-proton ratio at the top of the atmosphere, we corrected the number of selected antiprotons and protons for the production and loss of particles in the residual atmosphere above the apparatus as well as in the instrument itself. However, for obtaining antiproton-to-proton ratio, the selection efficiencies, which were considered to be the same for antiprotons and protons, were excluded from the calculation in order to reduce the errors. The resultant ratios are presented in Table 3.

Figure 10 shows the antiproton-to-proton ratio measured by CAPRICE98 along with other experimental data (Buffington et al. 1981; Golden et al. 1984; Bogomolov et al. 1987, 1990; Salomon et al. 1990; Stochaj et al. 1990; Mitchell et al. 1996; Boezio et al. 1997; Basini et al. 1999; Orito et al. 2000) and with theoretical calculations. The two solid lines show the upper and lower limit of a calculated flux of interstellar antiprotons by Simon, Molnar, & Roesler (1998) assuming a pure secondary production during the propagation of cosmic rays in the Galaxy . The dashed line shows a similar calculation by L. Bergström and P. Ullio (1999, private communication). It is worth noting that Simon et al. (1998) used the primary spectra measured by Menn et al.
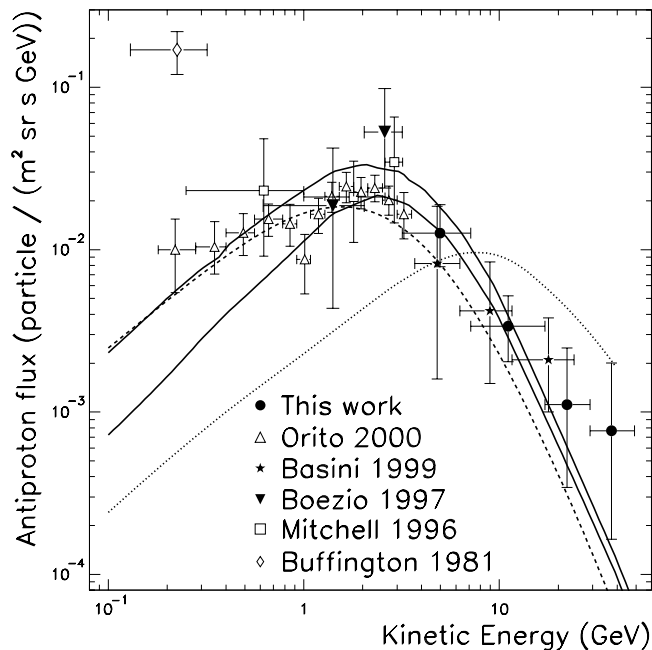

FIG. 9.—Antiproton flux at the top of the atmosphere obtained in this work and compared to other experiments that have published results on the antiproton flux (Buffington et al.1981; Mitchell et al. 1996; Boezio et al. 1997; Basini et al. 1999; Orito et al. 2000). The two solid lines shows the upper and lower limit of a calculated flux of interstellar secondary antiprotons by Simon et al. (1998). The dashed line shows the interstellar secondary antiproton flux calculated by L. Bergström & P. Ullio (1999, private communication). The dotted line shows the primary antiproton flux given by annihilation of neutralino from MSSM with a mass of 964 GeV (Ullio 1999).
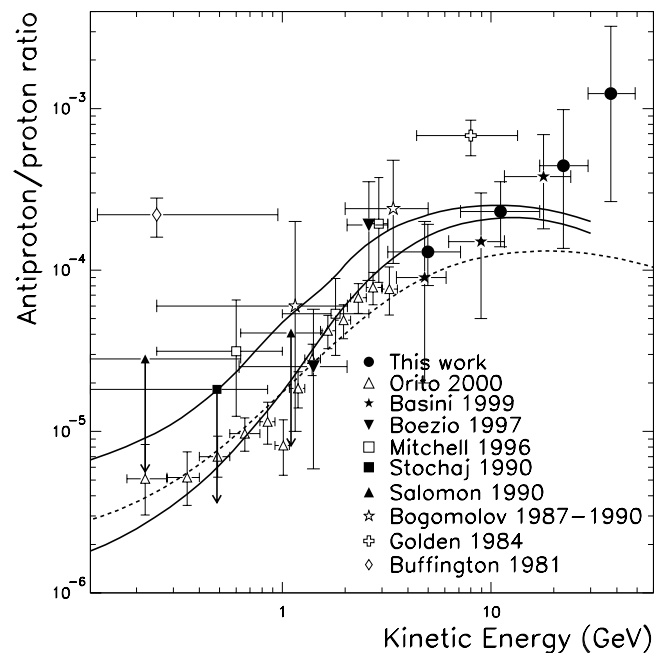

FIG. 10.—The $\bar{p}/p$ ratio at the top of the atmosphere obtained in this work compared with previous measurements (Buffington et al. 1981; Golden et al. 1984; Bogomolov et al. 1987, 1990; Salomon et al. 1990; Stochaj et al. 1990; Mitchell et al. 1996; Boezio et al. 1997; Basini et al. 1999; Orito et al. 2000). The lines are the calculations of interstellar antiprotons assuming a pure secondary production during the propagation of cosmic rays in the Galaxy by Simon et al. (1998; solid lines, upper and lower limits of the calculation) and by L. Bergström and P. Ullio (1999, private communication; dashed line).

(1997) and that L. Bergström and P. Ullio (1999, private communication) used the interstellar proton spectrum measured by Boezio et al. (1999).

The antiproton-to-proton ratio values presented here are in perfect agreement with the preliminary CAPRICE98 results published by Bergström et al. (2000). A small variation, of about a third of standard deviation, is found only for the highest energy bin essentially because of a better understanding of the proton spillover contamination.

5. SYSTEMATIC UNCERTAINTIES

Systematic errors originating from the determination of the detector efficiencies have already been discussed, and they have been included in the data in the figures and in the tables.

Another possible systematic error is related to the efficiency of the trigger system. The trigger efficiency was studied during the preflight preparations with a system measuring the coincidence of two scintillators placed above and below the top and bottom ToF scintillators. The efficiency was found to be close to 100% with an uncertainty of about 2%. The performance of the trigger system during the flight was also studied comparing the experimental spatial distribution of triggers with the distribution given by the same simulations as were used for the geometrical factor calculation, and an excellent agreement was found. Hence, the trigger efficiency could be assumed to be 100%, with a possible systematic uncertainty of less than 2%.

The method for calculating the geometrical factor used in this work was compared with two other techniques in the CAPRICE94 analysis (Boezio et al. 1999), and it was found to be in agreement within 2%, above 0.5 GV. Considering the similar geometrical configuration of CAPRICE98, it can be concluded that the uncertainty on values of the geometrical factor was about 2%.

Systematic errors owing to the uncertainty on the secondary production of antiprotons in the atmosphere were estimated comparing the results from the calculation by Stephens (1997), used in this work, with the independent calculation by Pfeifer, Roesler, & Simon (1996). It was found that the two calculations differ by $\simeq 22\%$ at 5 GeV decreasing to $\simeq 2\%$ above 8 GeV, with the calculation by Pfeifer et al. (1996) being the lower. This introduces an estimated uncertainty in the antiproton fluxes extrapolated to the top of the atmosphere, that is, $\simeq 6\%$ at 5 GeV decreasing to less than 1% above 8 GeV.

The atmospheric secondaries were also affected by the uncertainty in the residual atmosphere above the gondola. This was measured to be 5.5 g cm^{-2} by a pressure sensor owned and calibrated by the CAPRICE collaboration. The pressure was also measured by a detector owned and calibrated by the National Scientific Balloon Facility (NSBF). The NSBF pressure data were about 15% lower at float than the ones measured by our sensor. This results in an uncertainty on the antiproton fluxes of about 7% between 3 and 20 GeV decreasing to about 2% above 30 GeV.

The numbers of particles measured at the spectrometer were corrected for losses in the spectrometer and the atmosphere. Assuming a 10% uncertainty on the cross sections used in these calculations results in a systematic error on the antiproton fluxes of $\simeq 2\%$. An additional uncertainty of 1% should be considered due to the uncertainty on the atmospheric depths and the consequent effect on the losses in the atmosphere.

Assuming that the systematic errors were uncorrelated and, hence, could be quadratically summed, the resulting measurement of the antiproton flux includes systematic uncertainties that were energy-dependent decreasing from $\simeq 10\%$ at 5 GeV to $\simeq 8\%$ above 8 GeV and to $\simeq 4\%$ above 30 GeV.

Systematic uncertainties owing to the tracking system, caused by, for example, an offset in the deflection measurements, were analyzed using the RICH detector. The RICH high-Lorentz threshold for protons permitted to study several features of the tracking system up to a rigidity of about 100 GV (unattainable by previous cosmic rays experiments).

Figure 11a shows the Cherenkov angle resolution for protons obtained from flight data (filled circles) as a function of β, derived from the rigidity measured by the tracking system assuming the proton mass. The solid line indicates the measured resolution for muons (Bergström et al. 2001). The difference between the two resolutions was due to the finite resolution of the tracking system. In fact, this introduced an additional spread in the Cherenkov angle distribution when it was binned according to the β measured by the tracking system. The effect of this was more important for protons than for muons, since the rigidity (deflection) of the protons was nearly 10 times greater (smaller) than that of the muons, at the same β.

The effect of the tracking resolution of the binned Cherenkov angle distribution was obtained by simulating a large number of protons according to a power-law spectrum in rigidity with spectral index of -2.74. The corresponding Cherenkov angle was then calculated and smeared with a Gaussian distribution with a standard deviation given by the measured resolution for muons (Fig. 11a, solid line). Then the rigidity of each simulated proton was
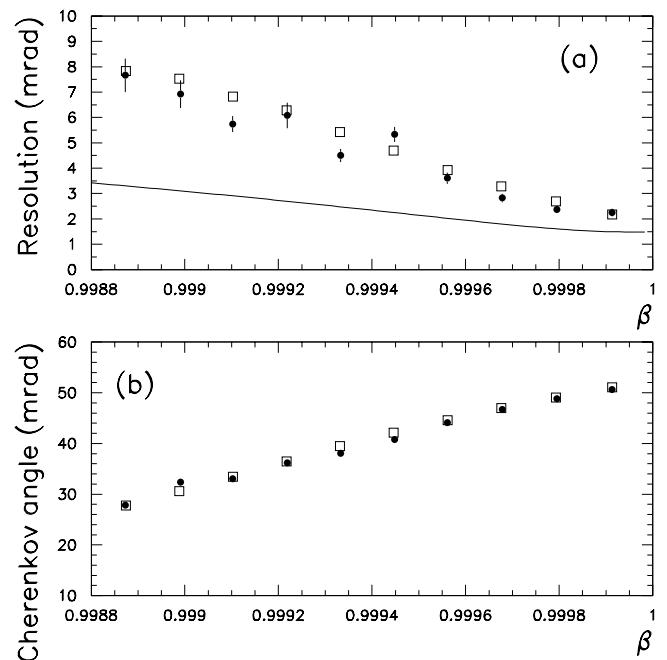

FIG. 11.—(a) Cherenkov angle resolution as a function of velocity for experimental (filled circles) and simulated protons (squares). The solid line is the experimental resolution for muons. (b) Mean Cherenkov angle as a function of velocity for experimental (filled circles) and simulated (squares) protons.

transformed to a corresponding deflection and smeared with values randomly picked from the tracking resolution function. The resulting deflection was then used to derive the velocity, which was used for the binning of the Cherenkov angles of these simulated events, similarly to the experimental case. The resulting Cherenkov angle resolution is shown as squares in Figure 11a. A good agreement was found between the measured and simulated resolutions. This was a strong indication that the tracking resolution function used in this work describes the tracking uncertainties with high precision and, consequently, could be used for determining the spillover proton contamination in the antiproton sample.

Figure 11b shows the measured mean Cherenkov angle (filled circles) as a function of β from the tracking system along with the simulated one (square). The same simulation was used as for the Cherenkov angle resolution. Also in this case, an excellent agreement was found. Furthermore, the comparison between the two sets of mean Cherenkov angle permitted limiting the possibility of an offset in the measured deflection, owing to effects such as wrong alignment of the drift chambers, positioning of the center of the magnet, mapping of the magnetic field, etc. An offset was introduced in the simulated deflection, and it was varied over a wide range of possible values. It was found that if an offset existed, at a 95% confidence level it was not larger than 0.001 $(GV)^{-1}$, which was significantly smaller than 0.003 $(GV)^{-1}$, corresponding to the MDR of the experiment (330 GV).

It is worth pointing out that the simulation was also tested with different spectral index such as -2.6 and -2.8, and no significant variation from the case presented here was found.

6. CONCLUSION

The antiproton flux and the antiproton-to-proton ratio have been determined in the energy region from 3 to 49 GeV by the CAPRICE98 experiment. This is the first time that the antiproton flux has been measured up to such high energies and over such a wide range in energy. Between 3 and 20 GeV our antiproton fluxes are consistent with the measurement by the MASS91 experiment (Basini et al. 1999). Both of these results, within the experimental errors, are also in agreement with the theoretical predictions by Simon et al. (1998) and L. Bergström and P. Ullio (1999, private communication), which assume a purely secondary origin of the cosmic-ray antiprotons. However, a primary component cannot be excluded, and the shape of the mea-

sured antiproton flux could indicate a presence of primary antiprotons. In fact, in the CAPRICE98 analysis we observed two antiproton events, with the highest energy antiproton measured at a kinetic energy of 43 GeV, between 29 and 49 GeV, while the expected number from a pure secondary origin is only 0.2–0.4 events, including muon contamination from the atmosphere; the lower and upper values correspond to the two extreme secondary curves of Figure 9. It is essential to improve the statistics on antiproton measurements in this high-energy region. In fact, the energy region studied here permits searching for specific signatures of neutralino-induced antiproton fluxes that are not attainable in lower energy regions. Furthermore, in this energy range nearly all calculations of interstellar secondary antiprotons in the literature are consistent with each other (Ullio 1999). These data are also substantially free of uncertainties owing to solar modulation effects.

As a continuation of its ballooning activity, the WiZard collaboration has developed a cosmic-ray experiment named PAMELA (Adriani et al. 1999) that will be launched in quasi-polar orbit on board of a Russian satellite at the beginning of 2003. PAMELA is based on a magnetic spectrometer with an MDR exceeding 800 GV and will determine the antiproton spectrum from 80 MeV, with a few orders of magnitude better statistics at energies above 5 GeV than the existing ones, free of the atmospheric background. Another cosmic-ray experiment, Alpha Magnetic Spectrometer (Ahlen et al. 1994), dedicated to the search for antinuclei, will be installed sometime later on the International Space Station. As it will have a similar MDR and will be based on the same set of detectors as PAMELA, it too will give further results on the study of high-energy antiprotons. Its much larger acceptance will also allow improvement to the statistics in the same high-energy range that will be explored by PAMELA.

REFERENCES

Adriani, O., et al. 1999, Proc. 26th Int. Cosmic-Ray Conf. (Salt Lake City), 5, 96
Ahlen, S., et al. 1994, Nucl. Instrum. Methods Phys. Res. A, 350, 351
Ambriola, M. L., et al. 1999, Nucl. Phys. B, 78, 32
Basini, G., et al. 1999, Proc. 26th Int. Cosmic-Ray Conf. (Salt Lake City), 3, 77
Bergström, D. 1999, Licentiat thesis, Royal Institute of Technology, Stockholm, Sweden
———. 2000, Ph.D. thesis, Royal Inst. Technology, Stockholm, Sweden
Bergström, D., et al. 2000, ApJ, 534, L177
———. 2001, Nucl. Instrum. Methods Phys. Res. A, in press
Bergström, L., Edsjö, J., & Ullio, P. 1999a, Phys. Rev. D, 59, 43506
———. 1999b, ApJ, 526, 215
Bocciolini, M., et al. 1993, Nucl. Instrum. Methods Phys. Res. A, 333, 560
———. 1996, Nucl. Instrum. Methods Phys. Res. A, 370, 403
Boezio, M. 1998, Ph.D. thesis, Royal Institute of Technology, Stockholm, Sweden
Boezio, M., et al. 1997, ApJ, 487, 415

Boezio, M., et al. 1999, ApJ, 518, 457
Bogomolov, E. A., et al. 1987, Proc. 20th Int. Cosmic-Ray Conf. (Moscow), 2, 72
———. 1990, Proc. 21st Int. Cosmic-Ray Conf. (Adelaide), 3, 288
Bottino, A., et al. 1998, Phys. Rev. D, 58, 123503
Brun, R., et al. 1994, GEANT, Detector Description and Simulation Tool, CERN Program Library (Geneva: CERN)
Buffington, A., Schindler, S. M., & Pennypacker, C. R. 1981, ApJ, 248, 1179
Carlson, P., et al. 1994, Nucl. Instrum. Methods Phys. Res. A, 349, 577
Francke, T., et al. 1999, Nucl. Instrum. Methods Phys. Res. A, 433, 87
Gleeson, L. J., & Axford, W. I. 1968, ApJ, 154, 1011
Golden, R. L., et al. 1978, Nucl. Instrum. Methods Phys. Res., 148, 179
———. 1979, Phys. Rev. Lett., 43, 1196
———. 1984, Astrophys. Lett., 24, 75
———. 1991, Nucl. Instrum. Methods Phys. Res. A, 306, 366
Hawking, S. W. 1974, Nature, 126, 30
Hof, M., et al. 1994, Nucl. Instrum. Methods Phys. Res. A, 345, 561
———. 1996, ApJ, 467, L33

Kiraly, P., Wdowczyk, J., & Wolfendale, A. 1981, Nature, 293, 120
Kremer, J., et al. 1999, Phys. Rev. Lett., 83, 4241
Lafferty, G. D., & Wyatt, T. T. 1995, Nucl. Instrum. Methods Phys. Res. A, 355, 541
Maki, K., Mitsui, T., & Orito, S. 1996, Phys. Rev. Lett., 76, 3474
Menn, W., et al. 1997, Proc. 25th Int. Cosmic-Ray Conf. (Durban), 3, 409
———. 2000, ApJ, 533, 281
Mitchell, J., et al. 1996, Phys. Rev. Lett., 76, 3057
Orito, S., et al. 2000, Phys. Rev. Lett., 84, 1078
Papini, P., Grimani, C., & Stephens, S. A. 1996, Nuovo Cimento C, 19, 367
Pfeifer, C., Roesler, S., & Simon, M. 1996, Phys. Rev. C, 54, 882
Ricci, M., et al. 1999, Proc. 26th Int. Cosmic-Ray Conf. (Salt Lake City), 5, 49

Salomon, S., et al. 1990, ApJ, 349, 78
Shea, M. A., & Smart, D. F. 1983, Proc. 18th Int. Cosmic-Ray Conf. (Bombay), 3, 411
Simon, M., Molnar, A., & Roesler, S. 1998, ApJ, 499, 250
Simpson, J. A., & Pyle, K. R. 1996, Space Physics Data System (Chicago: Univ. Chicago Press)
Stecker, F. W., Rudaz, S., & Walsh T. F. 1985, Phys. Rev. Lett., 55, 2622
Stephens, S. A. 1981, Proc. 17th Int. Cosmic-Ray Conf. (Paris), 4, 282
———. 1997, Astropart. Phys., 6, 229
Stochaj, S. J., et al. 1990, Proc. 21st Int. Cosmic-Ray Conf. (Adelaide), 3, 284
Sullivan, J. D. 1971, Nucl. Instrum. Methods, 95, 5
Ullio, P. 1999, astro-ph/9904086